J. Fluid Mech. (2024), *vol*. 982, A22, doi:10.1017/jfm.2024.64

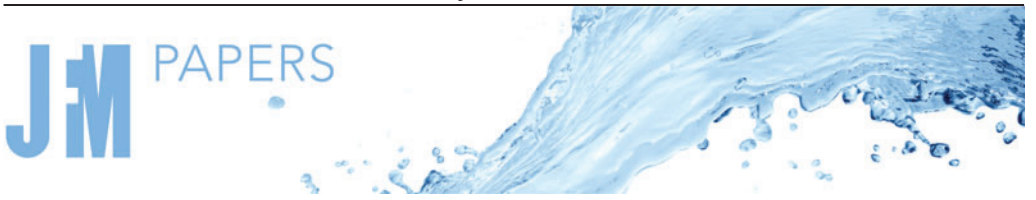

Short-wavelength instabilities in a finite-amplitude plane inertial wave

D.S. Abhiram[1,2] **and Manikandan Mathur**[1,2,†]

[1]Department of Aerospace Engineering, Indian Institute of Technology Madras, Chennai 600036, India

[2]Geophysical Flows Lab, Indian Institute of Technology Madras, Chennai 600036, India

(Received 10 June 2023; revised 4 December 2023; accepted 13 December 2023)

We perform a linear stability analysis of a finite-amplitude plane inertial wave (of frequency ω in the range $0 \leq \omega \leq f$, where f is the Coriolis frequency) by considering the inviscid evolution of three-dimensional (3-D), small-amplitude, short-wavelength perturbations. Characterizing the base flow plane inertial wave by its non-dimensional amplitude A and the angle Φ that its wavevector makes with the horizontal axis, the local stability equations are solved over the entire range of perturbation wavevector orientations. At sufficiently small A, 3-D parametric subharmonic instability (PSI) is the only instability mechanism, with the most unstable perturbation wavevector making an angle close to 60° with the inertial wave plane. In addition, the most unstable perturbation is shear-aligned with the inertial wave in the inertial wave plane. Further, at large Φ, i.e. $\omega \approx f$, there exists a wide range of perturbation wavevectors whose growth rate is comparable to the maximum growth rate. As A is increased, theoretical PSI estimates become less relevant in describing the instability characteristics, and the dominant instability transitions to a two-dimensional (2-D) shear-aligned instability, which is shown to be driven by third-order resonance. The transition from 3-D PSI to a 2-D shear-aligned instability is shown to be reasonably captured by two different criteria, one based on the nonlinear time scale in the inertial wave and the other being a Rossby-number-based one.

Key words: rotating flows, waves in rotating fluids

1. Introduction

Inertial waves are propagating disturbances in rotating flows, where the Coriolis force provides the restoring mechanism (Greenspan 1968; Pedlosky *et al.* 1987). They occur at

† Email address for correspondence: manims@smail.iitm.ac.in

frequencies ranging from zero to the Coriolis frequency, and are of dynamical significance in several natural systems where the background rotation is important, such as the Earth's core (Aldridge & Lumb 1987), ocean (Fu 1981) and atmosphere (Zhang & Yi 2007), as well as astrophysical flows (Ogilvie & Lin 2007; Favier *et al.* 2014; Ouazzani *et al.* 2020). Owing to their ability to transport significant momentum and energy across large distances, inertial waves are of importance in overall energy budgets and dynamical studies of the aforementioned natural systems. As a result, inertial wave generation and dissipation have been topics of several studies in the literature. One of the pathways for inertial wave dissipation is linear instability, which represents the focus of the current study.

Inertial wave dynamics has been studied both theoretically and experimentally in the last few decades. Early experimental studies were performed in finite-sized, closed rotating cylindrical tanks, where linear and nonlinear regimes of inertial wave modes were investigated (Greenspan 1969; McEwan 1970; Manasseh 1992; Kobine 1995). In these studies, nonlinear wave interactions, along with viscous boundary layer dynamics, were shown to play an important role in the associated mean circulation and breakdown of inertial waves into small-scale disorder. To understand these experimental observations, Kerswell (1999) performed a linear stability analysis of two representative inertial wave modes in confined cylindrical geometry to conclude that triadic resonances constitute the generic mechanism for secondary instability in rapidly rotating fluids. Motivated by applications in the Earth's core and tidally excited astrophysical bodies, inertial wave instabilities and associated mean flow dynamics have also been studied in spherical shells with precession and differential rotation (Lorenzani & Tilgner 2003; Wicht 2014; Hoff, Harlander & Egbers 2016*a*; Hoff, Harlander & Triana 2016*b*).

Our current study is motivated by inertial wave dynamics in the ocean, where a Cartesian geometry is suitable for describing processes that do not span several degrees in latitude or longitude. The primary source of inertial waves in the ocean is the winds, and it is now recognized that the energy input into wind-driven inertial waves with frequencies close to the local Coriolis frequency is comparable to the energy input into internal tides (Alford *et al.* 2016). Specifically, wind stress changes excite motions at frequencies close to the Coriolis frequency in the upper ocean, which could subsequently propagate as inertial waves. In addition, internal gravity waves excited by other mechanisms, such as tide–topography (Garrett & Kunze 2007) and flow–topography (Nikurashin & Ferrari 2010; Zemskova & Grisouard 2021) interactions, can also be significantly influenced by the background rotation and hence inertial wave dynamics (MacKinnon & Winters 2005).

One of the often-studied instability mechanisms in internal waves is the triadic resonance instability (TRI), where secondary waves with frequencies ω_1 and ω_2 and wavevectors $\boldsymbol{k}_1$ and $\boldsymbol{k}_2$ are excited, following $\omega_1 + \omega_2 = n\omega$ and $\boldsymbol{k}_1 + \boldsymbol{k}_2 = n\boldsymbol{k}$ (Drazin 1977). Here, ω and $\boldsymbol{k}$ are the primary wave frequency and wavevector, respectively, and $n + 1$ is the order of resonance (in the primary wave amplitude). A special case of TRI is the parametric subharmonic instability (PSI), where $n = 1$, $\omega_1 = \omega_2 = \omega/2$ and $\boldsymbol{k}_1 = -\boldsymbol{k}_2$ with $|\boldsymbol{k}_1| \gg |\boldsymbol{k}|$ (Staquet & Sommeria 2002). Recognizing that PSI is not well-understood in inertial waves, Bordes *et al.* (2012) studied the evolution of secondary subharmonic waves in inertial waves excited by a wave generator at laboratory scale. While triadic resonance was found to be the relevant mechanism of instability, viscous effects were shown to be important in the selection of secondary waves at the laboratory scale. In a more recent study, Mora *et al.* (2021) showed that the subharmonic waves produced by TRI do not propagate in the same vertical plane as the base inertial wave, thus establishing the three-dimensional (3-D) nature of TRI even at small primary wave amplitudes. Using classical triadic resonance equations for small primary wave amplitudes, Mora *et al.* (2021)

elucidated the 3-D nature of TRI in inertial waves. In this study, we perform a linear stability analysis of plane inertial waves using the local stability approach.

While Floquet theory has previously been used to study linear instabilities in spatially and temporally periodic internal waves (Mied 1976; Drazin 1977; Klostermeyer 1982; Sonmor & Klaassen 1997), the local stability approach is computationally efficient in exploring a wider range of base flow and perturbation parameters, and thereby identifying different instability mechanisms in various parameter regimes (Ghaemsaidi & Mathur 2019). The local stability analysis (Lifschitz & Hameiri 1991) considers the evolution of short-wavelength perturbations, for which the linear stability equations reduce to a set of ordinary differential equations that govern the evolution of the perturbation amplitude and wavevector along fluid particle trajectories in the base flow. It has been extensively used to investigate various instabilities in idealized models of vortices (Bayly 1986; Leblanc 1997; Sipp & Jacquin 2000), including the effects of background rotation (Godeferd, Cambon & Leblanc 2001) and stratification (Miyazaki & Fukumoto 1992; Aravind, Mathur & Dubos 2017).

The local stability approach has been used to study linear instabilities in waves too, with examples including Gerstner's waves (Leblanc 2004), equatorially trapped waves (Constantin & Germain 2013) and edge waves on a sloping beach (Ionescu-Kruse 2014). In the domain of internal waves in Cartesian geometry, it has been used to study standing inertial waves (Lifschitz & Fabijonas 1996), plane internal gravity waves (Ghaemsaidi & Mathur 2019), and standing and propagating inertia-gravity waves (Miyazaki & Adachi 1998). For standing inertial waves, Lifschitz & Fabijonas (1996) demonstrated that the growth rate tends to infinity as the amplitude and spatial scale of the inertial wave increases and decreases, respectively. In contrast to classical triadic resonance calculations, a linear stability analysis based on the local stability approach does not assume any specific instability mechanism; rather, instabilities such as TRI emerge as an outcome of the analysis. Furthermore, the linear stability analysis makes no assumptions about the amplitude of the base flow inertial wave, thus going beyond the small-amplitude inertial wave regime. Unlike the classical triadic resonance calculations, however, the local stability approach neglects the finite-wavenumber and viscous effects in the perturbations.

In the current study, we perform a local stability analysis of plane inertial waves to investigate linear instabilities associated with 3-D, short-wavelength perturbations. In addition to augmenting our understanding of previously observed characteristics of TRI in inertial waves, our study also explores the entire four-dimensional space occupied by inertial wave and perturbation parameters. Specifically, we obtain instability characteristics as a function of inertial wave amplitude/orientation and the orientation of the perturbation wavevector. The rest of the paper is organized as follows. Section 2 describes the base inertial wave and the local stability equations. Section 3 presents the growth rate variation as a function of various base flow and perturbation parameters, followed by an identification of various instability mechanisms in different regions of the parameter space. Section 4 summarizes the results and concludes with a discussion of the future scope of our study.

2. Theory

For an inviscid, incompressible flow with a uniform density ρ_0, the governing equations of motion in a rotating frame of reference are (Pedlosky *et al.* 1987)

$$\boldsymbol{\nabla} \cdot \boldsymbol{U} = 0, \tag{2.1}$$

$$\boldsymbol{U}_t + \boldsymbol{U} \cdot \boldsymbol{\nabla} \boldsymbol{U} + 2\boldsymbol{\Omega} \times \boldsymbol{U} = -\boldsymbol{\nabla}(p/\rho_0) - g\hat{\boldsymbol{e}}_z, \tag{2.2}$$

where $\boldsymbol{U}$ and p are the total velocity and pressure fields, respectively. Here $\boldsymbol{\Omega}$ is the constant background rotation, which we assume in this study to be $\boldsymbol{\Omega} = (f/2)\hat{\boldsymbol{e}}_z$. The acceleration due to gravity is g, which acts along $-\hat{\boldsymbol{e}}_z$. Decomposing the total flow into a base flow and a perturbation field (denoted by a prime), we write

$$\boldsymbol{U} = \bar{\boldsymbol{u}} + \boldsymbol{u}', \tag{2.3}$$

$$p = -\rho_0 g z + \bar{p} + p', \tag{2.4}$$

where the base flow is assumed to be a combination of quiescent flow with a hydrostatic pressure distribution and a plane inertial wave. Specifically, the velocity and pressure fields $\bar{\boldsymbol{u}}$ and $\bar{p}$ are described by a plane inertial wave, as discussed in § 2.1.

2.1. *Plane inertial wave*

A plane inertial wave, whose instability characteristics we study, can be described by

$$\bar{\psi} = \Psi \cos(kx + mz - \omega t), \tag{2.5}$$

$$\bar{p} = -\rho_0 \omega \Psi \cot \Phi \sin(kx + mz - \omega t), \tag{2.6}$$

$$\bar{v} = -\frac{f \Psi m}{\omega} \cos(kx + mz - \omega t), \tag{2.7}$$

where the stream function $\bar{\psi}$ specifies the horizontal and vertical velocity components as $(\bar{u}, \bar{w}) = (-\partial\bar{\psi}/\partial z, \partial\bar{\psi}/\partial x)$, $\bar{v}$ is the out-of-plane velocity component along the y-axis and $\bar{p}$ is the corresponding pressure field. Here Ψ is the stream function amplitude, and Φ represents the angle that the wavevector $\boldsymbol{k} = k\boldsymbol{e}_x + m\boldsymbol{e}_z$ makes with the x-axis. Based on the orthogonality between the phase and group velocities for a plane inertial wave, Φ can also be thought of as the angle made by the energy propagation direction with the vertical z-axis. We note here that the underlying mechanism that generates the plane inertial wave in (2.5)–(2.7) is not considered in the base flow for the stability analysis.

A schematic of the plane inertial wave is shown in figure 1. The wavenumbers (k, m) and the frequency ω are related by the dispersion relation (Greenspan 1968)

$$\sin^2 \Phi = \frac{m^2}{k^2 + m^2} = \frac{\omega^2}{f^2}. \tag{2.8}$$

As ω increases from zero to f, Φ increases from 0° to 90°. It is worth clarifying that the $\omega = f$ limit is referred to as the inertial wave in oceanography (Kunze & Sanford 1984), whereas we refer to the entire range of $0 \leq \omega \leq f$ as inertial waves. Choosing f^{-1} and $|\boldsymbol{k}|^{-1}$ as representative time and length scales, respectively, we define the following dimensionless parameters to characterize the base flow:

$$A = \frac{|\boldsymbol{k}|^2 \Psi}{f}, \quad \Phi = \tan^{-1}\left(\frac{m}{k}\right), \tag{2.9a,b}$$

where A and Φ are dimensionless parameters that characterize the inertial wave velocity amplitude and orientation, respectively. It is noteworthy that A is a Rossby number that represents the ratio between the internal wave shear in the x–z plane and the background rotation. In terms of the energy propagation direction (aligned with the group velocity

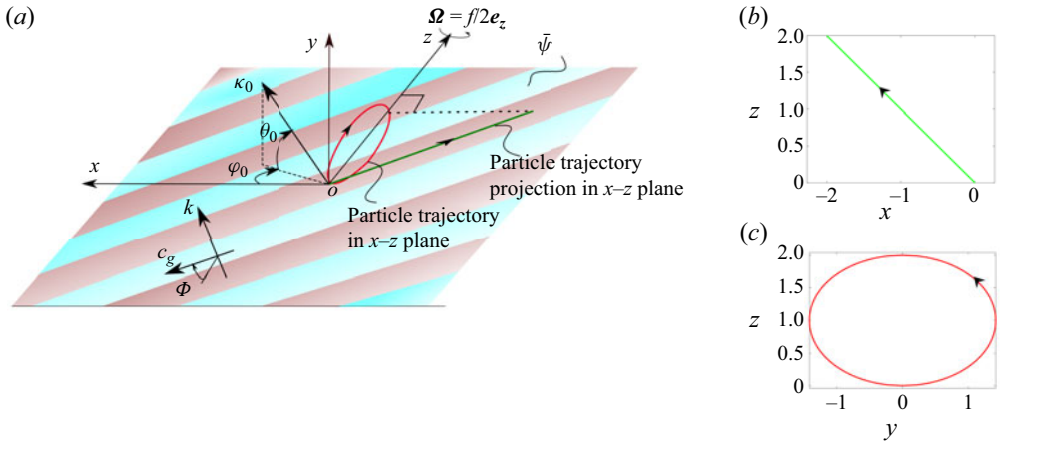

Figure 1. (*a*) Schematic depiction of the plane inertial wave with a wavevector $\boldsymbol{k}$ which is aligned at an angle Φ with the x-axis. The background is $\boldsymbol{\Omega} = f/2\boldsymbol{e}_z$. The projections of a representative fluid particle trajectory (not drawn to scale) on the y–z and x–z planes are shown in red and green, respectively. The initial perturbation wavevector κ_0 is aligned at an angle θ_0 with the x–z plane. The projection of κ_0 on the x–z plane makes an angle ϕ_0 with the x-axis. The projections of the representative fluid particle trajectory are also shown in panels (*b*) and (*c*).

vector, $\boldsymbol{c}_g$, shown in figure 1), smaller values of Φ correspond to steeper inertial waves. The corresponding non-dimensional velocity components in the x–z plane are

$$(\bar{u}, \bar{w}) = A \sin(x \cos \Phi + z \sin \Phi - t \sin \Phi)(\sin \Phi, -\cos \Phi). \tag{2.10}$$

In the rest of this paper, all the variables are non-dimensional. It is worth noting that the plane inertial wave in (2.5)–(2.7) is a solution of the fully nonlinear inviscid equations of motion (Craik & Criminale 1986), thus rendering our stability analysis valid even for finite-amplitude inertial waves.

2.2. *Local stability equations*

Following Lifschitz & Hameiri (1991), we write short-wavelength perturbations, which we superimpose onto the base flow, in the Wentzel–Kramers–Brillouin–Jeffreys form

$$(\boldsymbol{u}', p') = \exp(\mathrm{i}\Theta/\epsilon)[(\boldsymbol{a}, p) + \epsilon(\boldsymbol{a}_\epsilon, p_\epsilon) + \cdots], \tag{2.11}$$

where $a(\boldsymbol{x}, t)$ and $p(\boldsymbol{x}, t)$ are, respectively, the complex leading-order velocity and pressure perturbation amplitudes. Here $\Theta(x, t)$ is a real-valued phase function and ϵ is a small parameter representative of the ratio between the perturbation and the base flow inertial wavelength scales. Here $\boldsymbol{\kappa}(\boldsymbol{x}, t) = \nabla\Theta/\epsilon$ is the perturbation wavevector, which corresponds to short-wavelength perturbations owing to $\epsilon \ll 1$. Substituting equation (2.11) into (2.1) and (2.2) and gathering terms at $O(\epsilon^{-1})$ and $O(\epsilon^0)$, we obtain the local stability equations as (Godeferd *et al.* 2001; Nagarathinam, Sameen & Mathur 2015)

$$\frac{\mathrm{d}\boldsymbol{\kappa}}{\mathrm{d}t} = -(\nabla\bar{\boldsymbol{u}})^{\mathrm{T}} \cdot \boldsymbol{\kappa}, \tag{2.12}$$

$$\frac{\mathrm{d}\boldsymbol{a}}{\mathrm{d}t} = -\nabla\bar{\boldsymbol{u}} \cdot \boldsymbol{a} - \hat{\boldsymbol{e}}_z \times \boldsymbol{a} + \frac{\boldsymbol{\kappa}}{|\boldsymbol{\kappa}|^2}[2(\nabla\bar{\boldsymbol{u}} \cdot \boldsymbol{a}) \cdot \boldsymbol{\kappa} + (\hat{\boldsymbol{e}}_z \times \boldsymbol{a}) \cdot \boldsymbol{\kappa}], \tag{2.13}$$

where $\mathrm{d}/\mathrm{d}t = \partial/\partial t + \bar{\boldsymbol{u}} \cdot \nabla$ is the material time derivative along fluid particle trajectories in the base flow. Equations (2.12) and (2.13) represent the evolution of the perturbation

wavevector and leading-order velocity perturbation amplitude along fluid particle trajectories in the base flow $\bar{\boldsymbol{u}}$.

2.2.1. *Solution along an inertial wave trajectory*

In this subsection, we present analytical expressions for fluid particle trajectories in a plane inertial wave and discuss how to obtain solutions of (2.12) and (2.13) along specific fluid particle trajectories.

Defining $\beta = z_0 \sin\Phi + x_0 \cos\Phi$, where (x_0, z_0) is the initial position, the fluid particle trajectory $\bar{\boldsymbol{x}}(t) = (\bar{x}(t), \bar{y}(t), \bar{z}(t))$ in the plane inertial wave (2.10) is

$$[\bar{x}(t), \bar{z}(t)] = [x_0, z_0] + A[\cos(\beta - t\sin\Phi) - \cos\beta, -\cot\Phi(\cos(\beta - t\sin\Phi) - \cos\beta)], \tag{2.14a}$$

$$\bar{y}(t) = \frac{A}{\sin\Phi}(\sin(\beta - t\sin\Phi) - \sin\beta). \tag{2.14b}$$

Along the specific fluid particle trajectories represented by (2.14*a*,*b*), (2.12) and (2.13) reduce to ordinary differential equations with the dependent variables $\boldsymbol{\kappa}$ and a parameterized in terms of the only independent variable t.

Substituting equations (2.14*a*,*b*) and defining $\alpha = \kappa_{x0}\sin\Phi - \kappa_{z0}\cos\Phi$, the solution of (2.12) is

$$\begin{aligned}\boldsymbol{\kappa}(\bar{\boldsymbol{x}}(t), t) = \boldsymbol{\kappa_0} + A\{&\alpha(\sin(\beta - t\sin\Phi) - \sin\beta)\\ &+ \kappa_{y0}(\cos\beta - \cos(\beta - t\sin\Phi))\}[\cot\Phi, 0, 1],\end{aligned} \tag{2.15}$$

where

$$\boldsymbol{\kappa_0} = [\kappa_{x0}, \kappa_{y0}, \kappa_{z0}] = [\cos\theta_0\cos\phi_0, \sin\theta_0, \cos\theta_0\sin\phi_0], \tag{2.16}$$

is the initial perturbation wavevector. Here, θ_0 is the angle made by κ_0 with its projection on the (x, z) plane, and ϕ_0 is the angle that the projection of $\boldsymbol{\kappa_0}$ on the (x, z) plane makes with the x-axis. These angles are geometrically depicted in figure 1. Owing to the invariance of (2.12) and (2.13) with respect to a scaling of $\boldsymbol{\kappa}$ with any scalar, it suffices to consider initial perturbation wavevectors of unit magnitude (see (2.16)).

To obtain the growth rates for perturbations in a plane inertial wave of given (A, Φ), (2.13) is solved numerically for different values of (θ_0, ϕ_0) in the range of $\theta_0 \in [-90^\circ, 90^\circ]$ and $\phi_0 \in [0^\circ, 180^\circ]$. Integrating equation (2.13) for three different initial conditions, namely $a_{01} = [1, 0, 0]$, $a_{02} = [0, 1, 0]$ and $a_{03} = [0, 0, 1]$, Floquet theory is invoked to estimate the growth rate as

$$\sigma = \frac{\max(\mathrm{Re}(\log(\text{eigenvalues of } \boldsymbol{M})))}{2\pi/\sin\Phi}, \tag{2.17}$$

where $\boldsymbol{M} = [a_1; a_2; a_3]$. Here, a_1, a_2 and a_3 are the amplitude vectors obtained upon integrating equation (2.13) for one inertial wave time period $T = 2\pi/\sin\Phi$, using the initial conditions a_{01}, a_{02} and a_{03}, respectively. For the numerical integration of (2.13), the Runge–Kutta fourth-order scheme was used with a time step of $\delta t = T/1000$. This choice for δt ensured that the growth rates changed by less than 1 % when δt is halved. Finally, for a given (A, Φ), growth rates were calculated on an equispaced grid of 500 by 500 points on the (ϕ_0, θ_0) plane. The maximum growth rate on the (ϕ_0, θ_0) plane is denoted by σ^*, and the corresponding location is referred to as (ϕ_0^*, θ_0^*).

3. Results

We begin this section with results on the growth rate distributions in the parameter space of perturbation characteristics (§ 3.1). The growth rates at low and moderate inertial wave amplitudes are discussed within the context of PSI in § 3.2. Finally, in § 3.3, the dominant instability characteristics are presented and discussed.

3.1. *Growth rate distribution*

In figure 2, we present the growth rate σ on the (ϕ_0, θ_0) plane for nine different pairs of base flow parameters (A, Φ). The growth rate is periodic in ϕ_0 upon a flip in θ_0 such that $\sigma(\phi_0, \theta_0) = \sigma(180^\circ + \phi_0, -\theta_0)$. Interestingly, unlike for an internal wave with no background rotation (Ghaemsaidi & Mathur 2019), σ is not symmetric about $\theta_0 = 0$ for an inertial wave. The loss in symmetry can be understood as a consequence of the background rotation, as a result of which (2.12) and (2.13) are not invariant when θ_0 is replaced with $-\theta_0$. Specifically, it is already evident in the analytical solution for κ (see (2.15)) that replacing κ_{y0} with $-\kappa_{y0}$ non-trivially changes the evolution of κ_x and κ_y, and hence that of the perturbation wavevector orientation also. In figure 2, while the inertial wave amplitude varies from $A = 0.1$ to 1 to 10 from figure 2(*a–c*) to figure 2(*d–f*) to figure 2(*g–i*), the inertial wave orientation Φ varies from 15° to 45° to 75° from figure 2(*a*,*d*,*g*) to figure 2(*b*,*e*,*h*) to figure 2(*c*,*f*,*i*).

For $(A, \Phi) = (0.1, 15^\circ)$, clear instability band(s) are observed on the (ϕ_0, θ_0) plane (figure 2*a*). Asymmetry with respect to $\theta_0 = 0$ is noticeable, with the instability region in $\theta_0 > 0$ being thicker and stronger (in terms of the growth rate) overall. To investigate the relevance of PSI in describing the instability regions, we plot red dashed curves corresponding to

$$\phi_0 = \sin^{-1}\left(\frac{\sin\Phi}{2\cos\theta_0}\right) \quad \text{for } |\theta_0| \leq \cos^{-1}\left(\frac{\sin\Phi}{2}\right). \tag{3.1}$$

We note that the red dashed curves contain both the ϕ_0 in (3.1) and $180 - \phi_0$. Specifically, (3.1) identifies daughter inertial waves at frequency $\omega/2$ and with wavevector aligned with the perturbation wavevector $(\cos\theta_0 \cos\phi_0, \sin\theta_0, \cos\theta_0 \sin\phi_0)$. It is worth noting that (3.1) has made use of the 3-D inertial wave dispersion relation for the daughter wave,

$$\sin^2\phi_0 \cos^2\theta_0 = \frac{\kappa_{z0}^2}{|\kappa_0|^2} = \frac{\omega^2}{4f^2}. \tag{3.2}$$

In other words, the inertial waves with wavevectors $\kappa(\phi_0, \theta_0)$ and $\kappa(180 + \phi_0, -\theta_0)$, and both at frequencies $\omega/2$, are in triadic resonance with the primary inertial wave. The spatial triadic resonance condition is automatically satisfied up to leading order in ϵ since the two short-wavelength daughter waves are antiparallel to each other. We also recall from the beginning of this section that the growth rates corresponding to $\kappa(\phi_0, \theta_0)$ and $\kappa(180 + \phi_0, -\theta_0)$ are the same and can be considered as the corresponding PSI growth rate on the red dashed curves.

As seen in figure 2(*a*), the PSI curves are in a close neighbourhood of the instability regions and are strongly suggestive that the observed instabilities originate from PSI. To investigate this aspect further, we ran growth rate calculations at $(A, \Phi) = (0.01, 15^\circ)$, which showed that the PSI curves fall almost exactly on top of the instability regions, which have weaker growth rates compared with $(A, \Phi) = (0.1, 15^\circ)$. A quantitative comparison between growth rates from the local stability approach and PSI growth rates

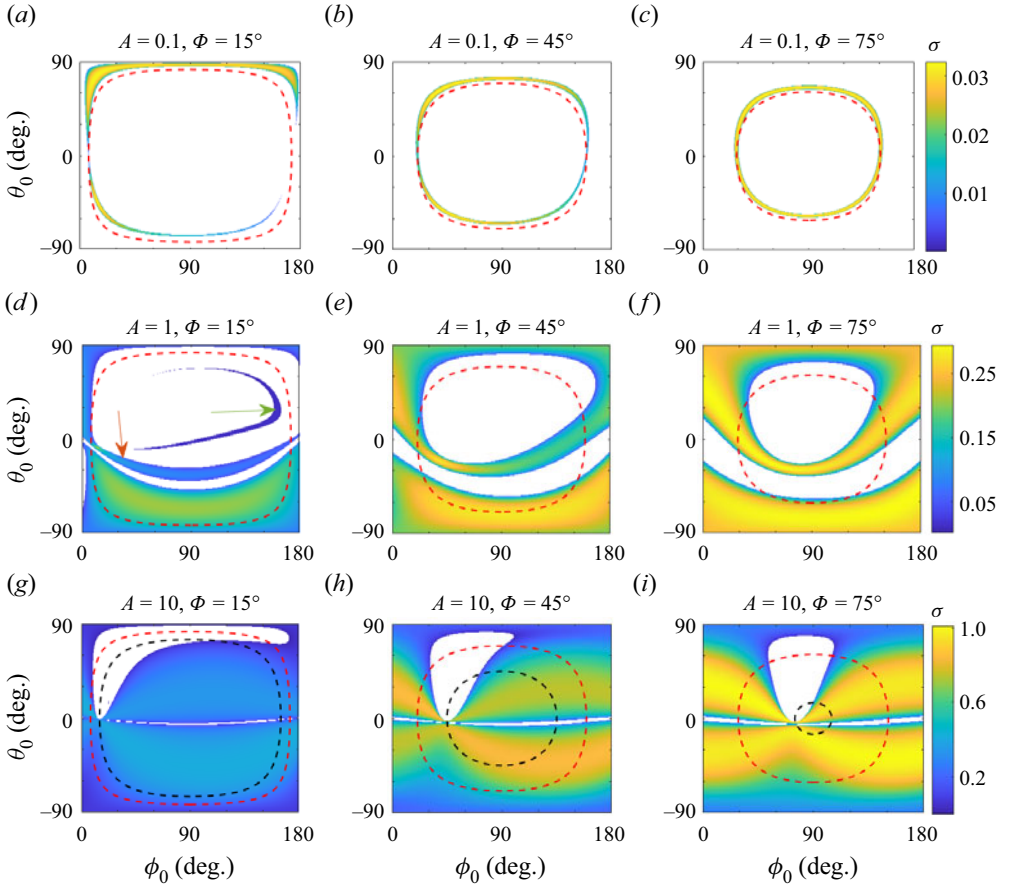

Figure 2. Growth rate (σ) as a function of ϕ_0 (deg.) and θ_0 (deg.) for $A = 0.1, 1, 10$ (*a–c*, *d–f*, *g–i*) and $\Phi = 15°, 45°, 75°$ (*a*,*d*,*g*, *b*,*e*,*h*, *c*,*f*,*i*). White regions correspond to $\sigma < 10^{-6}$. The red and black dashed curves represent the loci of the daughter waves corresponding to PSI of order two and three, respectively. The colour bar is common for all the figures in a given row.

based on classical triadic resonance calculations is presented later in this section (§ 3.2). In addition, growth rate calculations at different amplitudes in the local stability approach reveal that symmetry with respect to $\theta_0 = 0$ is progressively broken as we increase the amplitude from $A = 0$. As mentioned earlier, this could be attributed to the background rotation, which causes an out-of-plane velocity $\bar{v}$ that is proportional to A (see (2.7)).

Figure 2(*b*) shows the growth rate distribution for a shallower inertial wave corresponding to $(A, \Phi) = (0.1, 45°)$. In figure 2(*b*), σ is more symmetric with respect to $\theta_0 = 0$ than in figure 2(*a*). More interestingly, the PSI curves are nearly on top of the instability regions, thus reaffirming the relevance of PSI at small inertial wave amplitudes. This conclusion is further strengthened by the growth rate plot for the even shallower inertial wave corresponding to $(A, \Phi) = (0.1, 75°)$ shown in figure 2(*c*). In addition, the growth rate seems to vary only a little over the instability region for $(A, \Phi) = (0.1, 75°)$, whereas noticeable variations within the instability regions are observed for $(A, \Phi) = (0.1, 15°)$ and $(0.1, 45°)$. This aspect is further discussed in § 3.1. With respect to the location of maximum growth rate, the most unstable perturbations are clearly 3-D ($\theta_0 \neq 0$) for $(A, \Phi) = (0.1, 15°)$ and $(0.1, 45°)$, while two-dimensional (2-D) perturbations are

not far behind the most unstable 3-D perturbations for $(A, \Phi) = (0.1, 75^\circ)$. These observations for small-amplitude inertial waves are in contrast to small-amplitude internal waves, for which the most unstable perturbations are 2-D (Ghaemsaidi & Mathur 2019). The PSI in small-amplitude inertial waves is discussed in more detail in § 3.2. We now proceed to discuss the growth rate distribution on the (ϕ_0, θ_0) plane at larger inertial wave amplitudes.

Figure 2(*d–f*) show the growth rate distribution on the (ϕ_0, θ_0) plane for $(A, \Phi) = (1, 15^\circ)$, $(1, 45^\circ)$ and $(1, 75^\circ)$, respectively. As shown in figure 2(*d*), the unstable region in $\theta_0 < 0$ associated with PSI at $A = 0.1$ moves upwards and becomes thicker when A is increased to 1 (the region to which the 'red' arrow points). Interestingly, the theoretical PSI curve based on (3.1) is far from the aforementioned finite-amplitude extension of PSI. In addition, a seemingly new instability region that is attached to the $\theta_0 = -90^\circ$ axis appears at $A = 1$. Upon closer investigation, we found that this instability region is a continuous extension of the PSI region close to $\theta_0 = 90^\circ$. It is worth pointing out that $\theta_0 = -90^\circ$ and $\theta_0 = 90^\circ$ correspond to the same perturbation evolution equations since (2.12) and (2.13) are invariant under a scalar multiplication of $\boldsymbol{\kappa}$. Interestingly, if we assume the perturbations to follow the inertial dispersion relation in (3.2), $\theta_0 = \pm 90^\circ$ corresponds to zero frequency, i.e. a mean flow. The maximum growth rate occurs in this instability region that is attached to $\theta_0 = -90^\circ$, and the growth rate is close to its maximum over an extended region. For $\theta_0 > 0$, the unstable region associated with PSI is not too different between $A = 0.1$ and $A = 1$. Finally, it is also worthwhile to point out the appearance of a new, relatively thin unstable region (to which the 'green' arrow points) at $A = 1$, though the corresponding growth rates are small. In summary, for the finite-amplitude case of $(A, \Phi) = (1, 15^\circ)$, the PSI regions from small amplitude get significantly modified, and the most unstable perturbations occur in the $\theta_0 < 0$ finite-amplitude extension of PSI that occurs close to $\theta_0 = 90^\circ$ at smaller A. For larger Φ at $A = 1$ (figure 2*e*,*f*), the modifications to small-amplitude PSI are qualitatively similar to that for $\Phi = 15^\circ$. With respect to the most unstable perturbation wavevector, while it is possible to identify a location on the (ϕ_0, θ_0) plane where σ is maximum, a wide range of other wavevectors have similar growth rates as well, an aspect that was noted for $A = 0.1$ as well.

Increasing the inertial wave amplitude to $A = 10$, we plot the growth rate for $\Phi = 15^\circ$, 45° and 75° in figure 2(*g–i*), respectively. A significant portion of the (ϕ_0, θ_0) plane is now unstable. In the $\theta_0 < 0$ region, which is almost entirely unstable, extended regions correspond to relatively large growth rates. The theoretical PSI curve based on (3.1), shown in red, does not seem to be relevant in describing the unstable regions anymore. Interestingly, the maximum growth rate σ^* on the (ϕ_0, θ_0) plane seems to occur on the $\theta_0 = 0$ axis (2-D perturbations) for each of $\Phi = 15^\circ, 45^\circ, 75^\circ$. Furthermore, the corresponding $\phi_0 = \phi_0^*$ is not far from Φ for all three values of Φ. Physically, $\phi_0 = \Phi$ represents perturbations whose shear on the x–z plane aligns with the shear of the base flow inertial wave.

Motivated by the dominant instability being nearly 2-D and associated with shear-aligned perturbations at large A, we explored the relevance of third-order triadic resonance (Drazin 1977) in describing the dominant instability at large inertial wave amplitudes. In figure 2(*g–i*), the black dashed curves correspond to

$$\phi_0^* = \sin^{-1}\left(\frac{\sin\Phi}{\cos\theta_0}\right) \quad \text{for } |\theta_0| \leq \cos^{-1}(\sin\Phi), \tag{3.3}$$

which states that perturbations are at frequency ω and satisfy the 3-D inertial wave dispersion relation. Specifically, the secondary wave frequencies add up to 2ω for

third-order triadic resonance, thus satisfying the classical triadic resonance criteria (§ 1) at $n = 2$. The black dashed curves nearly pass through the maximum growth rate location in each of figure 2(*g–i*) and confirm that nearly 2-D, shear-aligned dominant instabilities at large A could indeed be a result of third-order triadic resonance. In § 3.2, we proceed to perform quantitative growth rate comparisons between local stability and classical triadic resonance calculations at small inertial wave amplitudes, and further explore the finite-amplitude extension of PSI based on the local stability analysis.

3.2. *Parametric subharmonic instability*

To quantify the relevance of PSI at small A, we perform comparisons with the growth rate of PSI as known from classical triadic resonance calculations. Based on triadic interaction equations in the inviscid limit, Mora *et al.* (2021) showed that the growth rate associated with short-wavelength daughter waves at half the primary wave frequency is given by

$$\sigma_{PSI} = \frac{A}{4}\sin\alpha_2(1+\cos\alpha_2), \tag{3.4}$$

where α_2 is the angle between the primary wavevector and one of the daughter waves. It is noteworthy that (3.4) assumes the primary wave amplitude to be sufficiently small, while the local stability approach makes no assumptions on A. Here σ_{PSI}/A is maximized for $\alpha_2 = 60^\circ$, thus allowing Mora *et al.* (2021) to conclude that PSI is strongest for 3-D daughter waves.

In figure 3(*a*), we plot σ/A as a function of α_2 from the local stability calculations for $\Phi = 15^\circ, 45^\circ$ and 75°. To enable comparisons with (3.4), which was derived for sufficiently small primary wave amplitudes, the local stability calculations were run at $A = 0.01$. Since the instability regions in the local stability approach need not coincide exactly with the theoretical PSI curves (recall results in figure 2*a–c*), we calculated the maximum σ in the vicinity of the theoretical PSI curves for the plot in figure 3(*a*). There is excellent quantitative agreement between σ and σ_{PSI} for the entire range of α_2, thus establishing that the local stability approach does indeed recover PSI in the small-amplitude limit. Interestingly, the range of α_2 decreases with Φ in figure 3(*a*). While α_2 ranges from 8° to 157° for $\Phi = 15^\circ$, it lies within the much smaller range of $[46^\circ, 76^\circ]$ for $\Phi = 75^\circ$. Given that σ_{PSI}/A depends only on α_2 at small A, it explains why the growth rate is nearly uniform throughout the theoretical PSI curve for $\Phi = 75^\circ$ in figure 2(*c*). In fact, this feature seems to extend to larger amplitudes too, where larger extended regions on the (ϕ_0, θ_0) plane have significant growth rates for larger Φ (see figure 2*d–f* and figure 2*g–i*).

To investigate the range of α_2 along the theoretical PSI curves for different Φ, we first plotted

$$\alpha_2 = \cos^{-1}(\cos\theta_0\cos(\phi_0 - \Phi)) \tag{3.5}$$

as a function of ϕ_0 and θ_0 (plot not shown here). Indeed, the range of α_2 on the entire (ϕ_0, θ_0) plane decreases with Φ. More importantly, contours of α_2 approach the theoretical PSI curve (see (3.1)) as Φ is increased. In the limit of $\Phi = 90^\circ$ (in other words, $\omega = f$), α_2 is uniformly 60° on the entire theoretical PSI curve. As a result, at $\Phi = 90^\circ$, σ_{PSI} is maximum for all the wavevectors along the PSI curve on the (ϕ_0, θ_0) plane. In summary, the range of perturbation wavevectors that have growth rates comparable to the maximum growth rate increases with Φ for small-amplitude inertial waves. In addition, the classical triadic resonance calculations for small-amplitude inertial waves predict that finite-wavenumber perturbations can have growth rates of the same order as

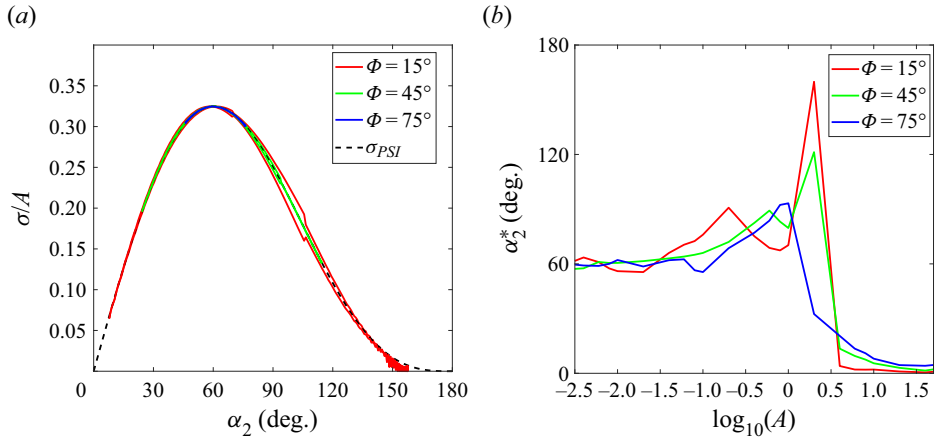

Figure 3. (*a*) Growth rate σ (normalized by A) as a function of α_2 for $\Phi = 15^\circ$ (red), 45° (green) and 75° (blue) based on the local stability calculations. The black dashed curve is based on classical triadic interaction equations (see (3.1)). (*b*) Plot of α_2^*, the value of α_2 at which σ is maximum, as a function of the inertial wave amplitude A for $\Phi = 15^\circ$ (red), 45° (green) and 75° (blue).

infinite-wavenumber perturbations (Mora *et al.* 2021). The local stability approach cannot recover such a result owing to its assumption of short-wavelength perturbations.

While PSI is the dominant mechanism at sufficiently small A and can be described well by classical triadic interaction equations, the instability characteristics get modified significantly as A is increased. To evaluate the validity of σ_{PSI} (see (3.4)) as A is increased, particularly its prediction that the maximum growth rate occurs at $\alpha_2 = 60^\circ$, we plot α_2^* as a function of A in figure 3(*b*). Here, α_2^* is based on the location (ϕ_0^*, θ_0^*) at which σ attains a maximum on the entire (ϕ_0, θ_0) plane for a given (A, Φ). Even at relatively small A, say $A \sim 0.1$, α_2^* clearly deviates from 60°, particularly for small Φ. The deviation continues to increase with A until we reach around $A = 1$, beyond which α_2^* rapidly decreases towards zero. While the rapid decrease towards zero is likely to be associated with a new instability mode, the PSI does seem to get significantly modified even for $A < 1$. The dominant instability characteristics are studied in more detail in § 3.3.

3.3. *Dominant instability characteristics*

For a given (A, Φ), the dominant instability is identified at the location (ϕ_0^*, θ_0^*) where σ attains a maximum on the entire (ϕ_0, θ_0) plane. The corresponding maximum growth rate is denoted by σ^*. Figure 4(*a*) shows the distribution of σ^* as a function of Φ and A. For a given Φ, σ^* monotonically increases with A, with σ^* being directly proportional to A for small A. Upon a closer look, we find that the increase in σ^* with A becomes slower than the small-amplitude regime at around $A = 0.1$, with the deviation from the small-amplitude regime occurring earlier for smaller Φ. With respect to variation with Φ, σ^* is nearly uniform for all Φ at small A, which is consistent with σ_{PSI}/A being dependent only on α_2 (see (3.4)) for small-amplitude inertial waves. Above a threshold $A \sim 1$, σ^* shows a clear monotonic increase with Φ.

For large A, the growth rates in figure 4(*a*) are large, and it is interesting to investigate their values relative to the base flow inertial wave frequency. With this motivation, we plot a rescaled growth rate $\bar{\sigma}^* = \sigma^*/\sin\Phi$, which represents the ratio between the maximum growth rate and the inertial wave frequency, in figure 5(*a*). At $A \sim 10$ or larger, $\bar{\sigma}^*$

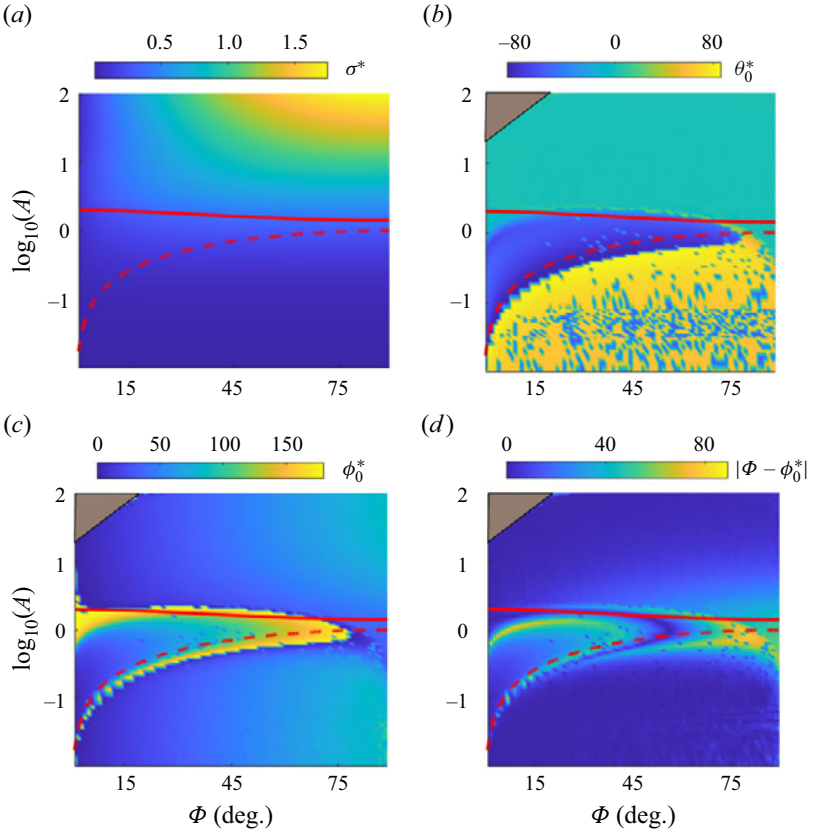

Figure 4. (*a*) Maximum growth rate σ^* as a function of Φ and A, and the corresponding (*b*) θ_0^* and (*c*) ϕ_0^* at which the maximum growth rate occurs. (*d*) Angle between the inertial wavevector and the most unstable perturbation wavevector, $|\Phi - \phi_0^*|$, as a function of Φ and A. The red dashed and solid lines in each plot correspond to $A/\sin\Phi = 1$ and $Ro = 2$, respectively, where Ro is defined in (3.6).

becomes greater than unity, indicating an instability that grows faster than the inertial wave frequency. As a result, the instability does not strongly feel the base flow inertial wave oscillations at sufficiently large A, and the dependence of $\bar{\sigma}^*$ on Φ becomes weaker than at small A. These results suggest that an asymptotic calculation at infinitesimally small ω, while allowing Φ to still vary from 0° to 90°, could be useful for understanding the instabilities at very large A. It should also be noted that the $\omega = 0$ limit (steady base flow, as discussed by Leblanc & Cambon (1997)) restricts the inertial wave orientation to $\Phi = 0$ and hence is not useful for capturing the dependence of $\bar{\sigma}^*$ on Φ at large A.

In figure 4(*b*), we plot θ_0^*, the initial angle made by the most unstable perturbation wavevector with the x–z plane, as a function of Φ and A. For small A, θ_0^* hovers around ±60° at all Φ, hence corresponding to strongly 3-D perturbations. We recall that σ_{PSI} (see (3.4)) is the same for $\pm\theta_0$, and this is at the origin of a noisy θ_0^* field when σ^* is detected numerically from the σ fields at small A. To circumvent this noise issue, we plot $||\theta_0^*| - 60°|$ in figure 5(*b*), which shows explicitly that θ_0^* hovers around ±60° for all Φ at small A. The closeness of θ_0^* to the optimum angle $\alpha_2 = 60°$ (see (3.5) for the definition of α_2) at which σ_{PSI} is maximum indicates that the corresponding ϕ_0^* is close to Φ, an aspect we will examine further in figure 4(*c*,*d*). As A is increased beyond $A \sim 0.1$, θ_0^* increases towards 90°, following which there is a sharp switch to $\theta_0^* = -90°$. This is related to the PSI branch

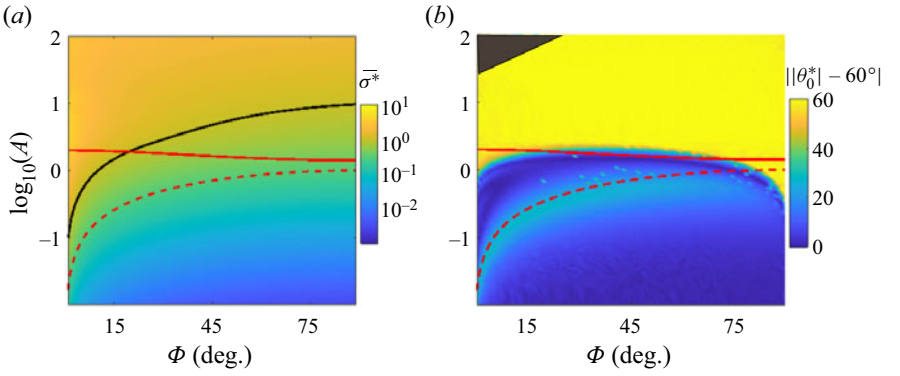

Figure 5. Plots of (*a*) $\bar{\sigma}^* = \sigma^*/\sin\Phi$ on a log scale and (*b*) $||\theta_0^*| - 60°|$ as a function of A and Φ. Here, θ_0^* is associated with the maximum growth rate σ^*, as plotted in figure 4(*a*,*b*), respectively. The red dashed and solid lines in each plot correspond to $A/\sin\Phi = 1$ and $Ro = 2$, respectively, where Ro is defined in (3.6). The black curve corresponds to $\bar{\sigma}^* = 1$.

in the $\theta_0 > 0$ region moving towards $\theta_0 = 90°$ and then appearing at $\theta_0 = -90°$, as shown in figure 2. Assuming the perturbations to follow the inertial wave dispersion relation (3.2), $\theta_0 = \pm 90°$ corresponds to zero frequency; in other words, at intermediate amplitudes, the dominant instability seems to be associated with the generation of an out-of-plane mean flow in the form of secondary perturbations. Following the switch to $\theta_0^* = -90°$, θ_0^* continues to increase with A. At around $A = 1$, there is another sharp change in θ_0^*, with its value rapidly going towards 0°, which represents 2-D perturbations. For larger A, θ_0^* continues to hover around 0°, suggesting that the dominant instability is nearly 2-D at sufficiently large inertial wave amplitudes.

Figure 4(*c*) shows the distribution of ϕ_0^*, the angle made by the projection of the most unstable perturbation wavevector on the x–z plane with the x-axis, as a function of Φ and A. Interestingly, ϕ_0^* monotonically increases with Φ in a similar manner at both small and large A. For intermediate values of A, ϕ_0^* seems to span the entire range of 0° to 180° as Φ is varied from 0° to 90°. Motivated by the variation of ϕ_0^* at small and large A, we plot the distribution of $|\Phi - \phi_0^*|$ in figure 4(*d*). Here $\Phi = \phi_0 *$ represents alignment between the wavevectors of the base flow inertial wave and the projection of the most unstable perturbation on the inertial wave plane. Hence, small values of $|\Phi - \phi_0^*|$ represent perturbations whose shear on the x–z plane is nearly aligned with the inertial wave shear. At sufficiently small and large A, $|\Phi - \phi_0^*|$ becomes nearly zero for all Φ. In other words, at sufficiently small A, the dominant instability is 3-D PSI (recall from figure 4*b* that θ_0^* is close to $\pm 60°$ at small A) with daughter waves whose shear on the (x, z) plane is nearly aligned with the inertial wave shear. At sufficiently large A, the dominant instability corresponds to 2-D, shear-aligned perturbations, which was interpreted as being driven by third-order triadic resonance in figure 2.

To develop an understanding of the observed transition from 3-D PSI to 2-D, shear-aligned instability, we explore the relevance of a criterion that compares the nonlinear time scale associated with an inertial wave with the inertial wave frequency. Specifically, the non-dimensional inertial wave amplitude A can be considered as the inverse of the nonlinear time scale (Yarom, Salhov & Sharon 2017), whereas $\sin\Phi = \omega/f$ is the inverse of the inertial wave time period. Interestingly, the criterion $A = \sin\Phi$, plotted as the red dashed curves in figure 4, seems to nearly capture the departure of the dominant instability from 3-D PSI at all Φ. In other words, the beginning of the

transition in the dominant instability mechanism as A is increased is driven by strongly nonlinear interactions becoming relevant at large A. To capture the end of the transition in the dominant instability mechanism, i.e. the dominant instability becoming 2-D and shear-aligned, we define a Rossby number Ro as

$$Ro = \frac{\sqrt{\max(\bar{u}^2 + \bar{v}^2)}|\boldsymbol{k}|}{f} = A\sqrt{1 + \sin^2 \Phi}, \tag{3.6}$$

where $\sqrt{\max(\bar{u}^2 + \bar{v}^2)}$ is the maximum velocity in the horizontal (x, y) plane for the inertial wave and $|\boldsymbol{k}|^{-1}$ is the chosen length scale. Interestingly, $Ro = 2$ (shown in red in figure 4*a–d*) seems to reasonably capture the transition to 2-D, shear-aligned instability, particularly at intermediate values of Φ. As a result, $A/\sin\Phi$ and Ro represent good measures of the dominant instability, though growth rates can be comparable to that of the dominant instability in extended portions of the (ϕ_0, θ_0) plane, as shown in figure 2. It is also interesting to note that the sufficient condition for inviscid instability in a steady, parallel shear flow with background rotation (Leblanc & Cambon 1997) reduces to $A\cos\Phi > 1$ if it were to be satisfied at some time during the inertial wave period. Such a criterion does not seem to be relevant in capturing the 3-D to 2-D instability transition in figure 4.

4. Conclusions

In this paper, a local stability analysis of plane inertial waves has been presented. Defining A and Φ as the non-dimensional amplitude and orientation (the angle between the energy propagation direction with the vertical) that characterize the base flow inertial wave, the local stability equations were numerically solved along fluid particle trajectories in the base flow. Specifically, the local stability framework was used to study the evolution of 3-D, small-amplitude perturbations on an inertial wave of arbitrary amplitude, thus going beyond the small-amplitude inertial wave regime that is often considered in the literature. Instability characteristics on the (ϕ_0, θ_0) plane were first plotted for representative small- to large-amplitude and steep to shallow inertial waves. Here, θ_0 is the angle made by the initial perturbation wavevector with the plane of the inertial wave, and ϕ_0 is the angle made by the projection (on the inertial wave plane) of the initial perturbation wavevector with the horizontal.

At small A, 3-D PSI is the dominant instability mechanism, and the local stability analysis recovers the results of Mora *et al.* (2021) based on classical triadic resonance equations for small-amplitude inertial waves. In addition, the local stability analysis revealed that at small A, the most unstable perturbation wavevector corresponds to $\theta_0 = \pm 60^\circ$, with its projection on the inertial wave plane being aligned with the wavevector of the inertial wave, i.e. shear-aligned. Furthermore, larger Φ corresponds to a larger proportion (of the theoretical PSI curve) of perturbation wavevectors whose growth rate is comparable to the maximum growth rate. In the limit of $\Phi = 90^\circ$, the growth rate is uniform over the entire theoretical PSI curve on the (ϕ_0, θ_0) plane (see the Appendix). As a result, the $\omega \approx f$ regime, which is particularly relevant and referred to as 'near-inertial' in oceanography, a continuous range of secondary waves could be excited as a result of PSI. These observations for small-amplitude inertial waves are in contrast to small-amplitude internal waves, for which the most unstable perturbations are 2-D (Ghaemsaidi & Mathur 2019). As A is increased, strong asymmetry about $\theta_0 = 0$ develops in the instability characteristics, and the theoretical PSI curves lose their relevance in describing the finite-amplitude extension of PSI. At large A, 2-D shear-aligned instabilities

driven by third-order triadic resonance are dominant, though significant growth rates occur over extended regions on the (ϕ_0, θ_0) plane. The transition from 3-D PSI at small A to 2-D shear-aligned instability at large A is captured reasonably well by $A/\sin\Phi = 1$ and $Ro = 2$. Here, $A/\sin\Phi$ is a measure of the smallness of the nonlinear time scale relative to the inertial wave time period, and Ro (see (3.6)) is a Rossby number defined based on the horizontal velocity and wavevector magnitude of the inertial wave. It is unclear why Ro is the relevant Rossby number to capture the transition to 2-D, shear-aligned instability, and an analytical calculation around 2-D, shear-aligned instability could be insightful.

In the future, it would be interesting to validate the results from our study using direct numerical simulations (see Onuki, Joubaud & Dauxois (2021) for an example of such a simulation in an internal gravity wave), which could also be used to explore nonlinear regimes of the linear instabilities reported here. The overall instability diagram that depicts the dominant instabilities over a wide range of inertial wave parameters is also a useful tool for designing and interpreting experiments and numerical simulations, especially those aimed at understanding how the driving instabilities influence the nature of resulting turbulence and mixing. Depending on the specific values of A and Φ, our results also highlight that a wide range of perturbation wavevectors could have similar growth rates, potentially an important consideration from the wave turbulence perspective on nonlinear regimes in inertial waves (Yarom & Sharon 2014; Monsalve *et al.* 2020). For oceanic applications, such as inertial waves excited by winds (Moehlis & Llewellyn Smith 2001; Mahadevan & Tandon 2006), the local stability analysis presents a useful tool for evaluating the possibility of local instabilities being a pathway towards dissipation. To increase the relevance to realistic oceanic settings, it would be insightful to extend the local stability calculations to the case of inertia-gravity waves, where both rotation and stratification are dynamically important. It is worthwhile to recall that the local stability approach has previously been used in idealized vortex models with background rotation and stratification (Miyazaki 1993; Nagarathinam *et al.* 2015). Finally, for astrophysical applications, it would perhaps be useful to perform a local stability analysis on inertial waves in spherical geometry.

Funding. D.S.A. thanks the PMRF scheme of the Ministry of Education, Government of India, for its support. The authors thank the Department of Science and Technology, India (FIST grant SR/FST/ET-II/2017/109) and the National Centre for Polar and Ocean Research (grant no. NCPOR/2019/PACER-POP/OS-05) for their support. This work was supported in part by the Collaborative Research Program of the Research Institute for Applied Mechanics, Kyushu University, Japan, and also benefited from discussions with Yohei Onuki.

Declaration of interests. The authors report no conflict of interest.

Author ORCIDs.
D.S. Abhiram https://orcid.org/0009-0001-1378-2182;
Manikandan Mathur https://orcid.org/0000-0002-2133-3889.

Appendix

In this appendix, we plot the growth rate distribution on the plane of perturbation wavevector orientations (ϕ_0, θ_0) in the limit of $\omega = f$, i.e. $\Phi = 90^\circ$ (the so-called inertial limit in the oceanography literature), and $A = 0.1$ (figure 6). As was observed for $\Phi = 75^\circ$, the theoretical PSI curve is in a close vicinity of the unstable region for $\Phi = 90^\circ$ too. Interestingly, the theoretical PSI curves for $\Phi = 75^\circ$ and 90° are not too far from each other. It is also noteworthy that the growth rate is nearly uniform all along the unstable region for $A = 0.1$ and $\Phi = 90^\circ$.

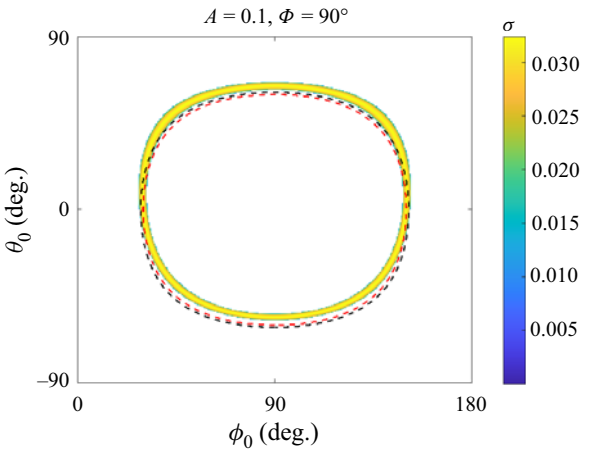

Figure 6. Growth rate (σ) as a function of ϕ_0 (deg.) and θ_0 (deg.) for $A = 0.1$ and $\Phi = 90^\circ$. White regions correspond to $\sigma < 10^{-6}$. The red and black dashed curves represent the loci of the daughter waves corresponding to PSI of order two for $\Phi = 90^\circ$ and $\Phi = 75^\circ$, respectively.

References

Aldridge, K.D. & Lumb, L.I. 1987 Inertial waves identified in the Earth's fluid outer core. *Nature* **325** (6103), 421–423.

Alford, M.H., MacKinnon, J.A., Simmons, H.L. & Nash, J.D. 2016 Near-inertial internal gravity waves in the ocean. *Annu. Rev. Mar. Sci.* **8**, 95–123.

Aravind, H.M., Mathur, M. & Dubos, T. 2017 Short-wavelength secondary instabilities in homogeneous and stably stratified shear flows. arXiv:1712.05868.

Bayly, B.J. 1986 Three-dimensional instability of elliptical flow. *Phys. Rev. Lett.* **57** (17), 2160.

Bordes, G., Moisy, F., Dauxois, T. & Cortet, P.-P. 2012 Experimental evidence of a triadic resonance of plane inertial waves in a rotating fluid. *Phys. Fluids* **24** (1), 014105.

Constantin, A. & Germain, P. 2013 Instability of some equatorially trapped waves. *J. Geophys. Res. Oceans* **118** (6), 2802–2810.

Craik, A.D.D. & Criminale, W.O. 1986 Evolution of wavelike disturbances in shear flows: a class of exact solutions of the Navier–Stokes equations. *Proc. R. Soc. Lond.* A. *Math. Phys. Sci.* **406** (1830), 13–26.

Drazin, P.G. 1977 On the instability of an internal gravity wave. *Proc. R. Soc. Lond.* A. *Math. Phys. Sci.* **356** (1686), 411–432.

Favier, B., Barker, A.J., Baruteau, C. & Ogilvie, G.I. 2014 Non-linear evolution of tidally forced inertial waves in rotating fluid bodies. *Mon. Not. R. Astron. Soc.* **439** (1), 845–860.

Fu, L.-L. 1981 Observations and models of inertial waves in the deep ocean. *Rev. Geophys.* **19** (1), 141–170.

Garrett, C. & Kunze, E. 2007 Internal tide generation in the deep ocean. *Annu. Rev. Fluid Mech.* **39**, 57–87.

Ghaemsaidi, S.J. & Mathur, M. 2019 Three-dimensional small-scale instabilities of plane internal gravity waves. *J. Fluid Mech.* **863**, 702–729.

Godeferd, F.S., Cambon, C. & Leblanc, S. 2001 Zonal approach to centrifugal, elliptic and hyperbolic instabilities in Stuart vortices with external rotation. *J. Fluid Mech.* **449**, 1–37.

Greenspan, H.P. 1968 The theory of rotating fluids. *Tech. Rep*. Massachusetts Institute of Technology Department of Mathematics.

Greenspan, H.P. 1969 On the non-linear interaction of inertial modes. *J. Fluid Mech.* **36** (2), 257–264.

Hoff, M., Harlander, U. & Egbers, C. 2016*a* Experimental survey of linear and nonlinear inertial waves and wave instabilities in a spherical shell. *J. Fluid Mech.* **789**, 589–616.

Hoff, M., Harlander, U. & Triana, S.A. 2016*b* Study of turbulence and interacting inertial modes in a differentially rotating spherical shell experiment. *Phys. Rev. Fluids* **1** (4), 043701.

Ionescu-Kruse, D. 2014 Instability of edge waves along a sloping beach. *J. Differ. Equ.* **256** (12), 3999–4012.

Kerswell, R.R. 1999 Secondary instabilities in rapidly rotating fluids: inertial wave breakdown. *J. Fluid Mech.* **382**, 283–306.

KLOSTERMEYER, J. 1982 On parametric instabilities of finite-amplitude internal gravity waves. *J. Fluid Mech.* **119**, 367–377.
KOBINE, J.J. 1995 Inertial wave dynamics in a rotating and precessing cylinder. *J. Fluid Mech.* **303**, 233–252.
KUNZE, E. & SANFORD, T.B. 1984 Observations of near-inertial waves in a front. *J. Phys. Oceanogr.* **14** (3), 566–581.
LEBLANC, S. 1997 Stability of stagnation points in rotating flows. *Phys. Fluids* **9** (11), 3566–3569.
LEBLANC, S. 2004 Local stability of Gerstner's waves. *J. Fluid Mech.* **506**, 245–254.
LEBLANC, S. & CAMBON, C. 1997 On the three-dimensional instabilities of plane flows subjected to Coriolis force. *Phys. Fluids* **9** (5), 1307–1316.
LIFSCHITZ, A. & FABIJONAS, B. 1996 A new class of instabilities of rotating fluids. *Phys. Fluids* **8** (8), 2239–2241.
LIFSCHITZ, A. & HAMEIRI, E. 1991 Local stability conditions in fluid dynamics. *Phys. Fluids* A*: Fluid Dyn.* **3** (11), 2644–2651.
LORENZANI, S. & TILGNER, A. 2003 Inertial instabilities of fluid flow in precessing spheroidal shells. *J. Fluid Mech.* **492**, 363–379.
MACKINNON, J.A. & WINTERS, K.B. 2005 Subtropical catastrophe: significant loss of low-mode tidal energy at 28.9°. *Geophys. Res. Lett.* **32** (15), L15605.
MAHADEVAN, A. & TANDON, A. 2006 An analysis of mechanisms for submesoscale vertical motion at ocean fronts. *Ocean Model.* **14** (3-4), 241–256.
MANASSEH, R. 1992 Breakdown regimes of inertia waves in a precessing cylinder. *J. Fluid Mech.* **243**, 261–296.
MCEWAN, A.D. 1970 Inertial oscillations in a rotating fluid cylinder. *J. Fluid Mech.* **40** (3), 603–640.
MIED, R.P. 1976 The occurrence of parametric instabilities in finite-amplitude internal gravity waves. *J. Fluid Mech.* **78** (4), 763–784.
MIYAZAKI, T. 1993 Elliptical instability in a stably stratified rotating fluid. *Phys. Fluids* A*: Fluid Dyn.* **5** (11), 2702–2709.
MIYAZAKI, T. & ADACHI, K. 1998 Short-wavelength instabilities of waves in rotating stratified fluids. *Phys. Fluids* **10** (12), 3168–3177.
MIYAZAKI, T. & FUKUMOTO, Y. 1992 Three-dimensional instability of strained vortices in a stably stratified fluid. *Phys. Fluids* A*: Fluid Dyn.* **4** (11), 2515–2522.
MOEHLIS, J. & LLEWELLYN SMITH, S.G. 2001 Radiation of mixed layer near-inertial oscillations into the ocean interior. *J. Phys. Oceanogr.* **31** (6), 1550–1560.
MONSALVE, E., BRUNET, M., GALLET, B. & CORTET, P.-P. 2020 Quantitative experimental observation of weak inertial-wave turbulence. *Phys. Rev. Lett.* **125** (25), 254502.
MORA, D.O., MONSALVE, E., BRUNET, M., DAUXOIS, T. & CORTET, P.-P. 2021 Three-dimensionality of the triadic resonance instability of a plane inertial wave. *Phys. Rev. Fluids* **6** (7), 074801.
NAGARATHINAM, D., SAMEEN, A. & MATHUR, M. 2015 Centrifugal instability in non-axisymmetric vortices. *J. Fluid Mech.* **769**, 26–45.
NIKURASHIN, M. & FERRARI, R. 2010 Radiation and dissipation of internal waves generated by geostrophic motions impinging on small-scale topography: theory. *J. Phys. Oceanogr.* **40** (5), 1055–1074.
OGILVIE, G.I. & LIN, D.N.C. 2007 Tidal dissipation in rotating solar-type stars. *Astrophys. J.* **661** (2), 1180.
ONUKI, Y., JOUBAUD, S. & DAUXOIS, T. 2021 Simulating turbulent mixing caused by local instability of internal gravity waves. *J. Fluid Mech.* **915**, A77.
OUAZZANI, R.-M., LIGNIÈRES, F., DUPRET, M.-A., SALMON, S.J.A.J., BALLOT, J., CHRISTOPHE, S. & TAKATA, M. 2020 First evidence of inertial modes in γ Doradus stars: the core rotation revealed. *Astron. Astrophys.* **640**, A49.
PEDLOSKY, J., *et al.* 1987 *Geophysical Fluid Dynamics*. Springer.
SIPP, D. & JACQUIN, L. 2000 Three-dimensional centrifugal-type instabilities of two-dimensional flows in rotating systems. *Phys. Fluids* **12** (7), 1740–1748.
SONMOR, L.J. & KLAASSEN, G.P. 1997 Toward a unified theory of gravity wave stability. *J. Atmos. Sci.* **54** (22), 2655–2680.
STAQUET, C. & SOMMERIA, J. 2002 Internal gravity waves: from instabilities to turbulence. *Annu. Rev. Fluid Mech.* **34** (1), 559–593.
WICHT, J. 2014 Flow instabilities in the wide-gap spherical Couette system. *J. Fluid Mech.* **738**, 184–221.
YAROM, E., SALHOV, A. & SHARON, E. 2017 Experimental quantification of nonlinear time scales in inertial wave rotating turbulence. *Phys. Rev. Fluids* **2** (12), 122601.
YAROM, E. & SHARON, E. 2014 Experimental observation of steady inertial wave turbulence in deep rotating flows. *Nat. Phys.* **10** (7), 510–514.

ZEMSKOVA, V.E. & GRISOUARD, N. 2021 Near-inertial dissipation due to stratified flow over abyssal topography. *J. Phys. Oceanogr.* **51** (8), 2483–2504.

ZHANG, S.D. & YI, F. 2007 Latitudinal and seasonal variations of inertial gravity wave activity in the lower atmosphere over central China. *J. Geophys. Res.: Atmos.* **112** (D5), D05109.